

A WRF-Based Tool for Forecast Sensitivity to the Initial Perturbation: The Conditional Nonlinear Optimal Perturbations versus the First Singular Vector Method and Comparison to MM5

HUIZHEN YU,^{a,b} HONGLI WANG,^{c,d} ZHIYONG MENG,^a MU MU,^e XIANG-YU HUANG,^f
AND XIN ZHANG^g

^a *Laboratory for Climate and Ocean–Atmosphere Studies, Department of Atmospheric and Oceanic Sciences, School of Physics, Peking University, Beijing, China*

^b *Qingdao Meteorological Bureau, Shandong, China*

^c *Cooperative Institute for Research in the Atmosphere, Colorado State University, Fort Collins, Colorado*

^d *Global Systems Division, NOAA/Earth System Research Laboratory, Boulder, Colorado*

^e *Institute of Atmospheric Sciences, Fudan University, Shanghai, China*

^f *Centre for Climate Research Singapore, Meteorological Service Singapore, Singapore*

^g *IBM Research–China, Beijing, China*

(Manuscript received 12 September 2015, in final form 22 October 2016)

ABSTRACT

A forecast sensitivity to initial perturbation (FSIP) analysis tool for the WRF Model was developed. The tool includes two modules respectively based on the conditional nonlinear optimal perturbation (CNOP) method and the first singular vector (FSV) method. The FSIP tool can be used to identify regions of sensitivity for targeted observation research and important influential weather systems for a given forecast metric.

This paper compares the performance of the FSIP tool to its MM5 counterpart, and demonstrates how CNOP, local CNOP (a kind of conditional nonlinear suboptimal perturbation), and FSV were detected using their evolutions of cost function. The column-integrated features of the perturbations were generally similar between the two models. More significant differences were apparent in the details of their vertical distribution. With Typhoon Matsa (2005) in the western North Pacific and a winter storm in the United States (2000) as validation cases, this work examined the tool's capability to identify sensitive regions for targeted observation and to investigate important influential weather systems. The location and pattern of the sensitive areas identified by CNOP, local CNOP, and FSV were quite similar for both the Typhoon Matsa case and the winter storm case. The main differences were mainly in their impact on the growth of forecast difference and the details of their vertical distributions. For both cases, the wind observations might be more important than temperature observations. The results also showed that local CNOP was more capable of capturing the influence of important weather systems on the forecast of total dry energy in the verification area.

1. Introduction

The question of predictability in the atmospheric sciences has received considerable attention since the work of Lorenz (1963, 1975). Sensitivity analysis, which examines, but is not limited to, the forecast response to a change in the initial conditions, is one way to study predictability, and a potential application of sensitivity

analysis is targeted observation. Targeted observation is a method in which a special area is determined to gather extra observations that provide the optimal decrease in error of a certain forecast metric through assimilating those extra observations. The method has attracted considerable attention since it was first proposed by Snyder (1996; e.g., Aberson 2003, 2011; Peng and Reynolds 2005, 2006; Wu et al. 2007, 2009b), and encouraging results have been obtained in a series of field experiments, such as the Fronts and Atlantic Storm Track Experiment (FASTEX; Bergot 1999) and the North Pacific Experiment (NORPEX; Langland et al. 1999). Targeting strategies can be roughly classified into

 Denotes Open Access content.

Corresponding author e-mail: Dr. Zhiyong Meng, zymeng@pku.edu.cn

DOI: 10.1175/JTECH-D-15-0183.1

© 2017 American Meteorological Society

two groups—one based on adjoint technology, such as singular vectors (SVs; Palmer et al. 1998), and the other encompassing ensemble-based methods, such as the ensemble transform Kalman filter (Bishop et al. 2001).

A common limitation of most current targeting strategies based on adjoint techniques is that the magnitude of the initial perturbation needs to be sufficiently small to make sure the error propagation feature in the original nonlinear model can be approximated by the error propagation feature in the tangent linear model. The SV method is one such strategy and has been widely used (Bergot 1999; Reynolds and Rosmond 2003). However, in the situations when the initial error is large, the application of the adjoint methods to targeted observation will break down. This issue is quite serious for mesoscale weather systems due to the sparse observations.

To take nonlinearity into account, Mu and Duan (2003) proposed the conditional nonlinear optimal perturbation (CNOP) strategy. The CNOP method is essentially a nonlinear extension of the first singular vector (FSV) method. CNOP is defined as the initial perturbation whose nonlinear evolution attains the maximum of a cost function under certain physical constraints over a chosen period (Mu and Duan 2003). This idea was also applied in the study of the transition-to-turbulence problem in fluid mechanics (Kerswell et al. 2014).

CNOP has been widely used to identify areas of sensitivity in targeted observations for mesoscale and tropical cyclone forecasts. The results showed that the deployment of additional observations in the sensitive area identified by CNOP had an overall positive influence on typhoon track forecasts, and the degree of improvement was generally larger than that based on the FSV method (Mu et al. 2007, 2009; Chen 2011; Qin and Mu 2012; Chen et al. 2013; Qin et al. 2013).

Besides identifying the most sensitive area to add extra observations for initialization in numerical weather prediction, sensitivity analysis can also be used to identify precursors of a weather system or to examine the possible interaction between different synoptic systems (Wu et al. 2007, 2009a), which could be quite useful for identifying key contributors to a weather event, especially from an operational forecasting point of view. The results of Wu et al. (2009b) showed that adjoint-based methods could capture the signal of the related dynamic systems that may affect typhoon movement or evolution. CNOP has also been applied in the studies of weather and climate predictability (Mu and Duan 2003; Duan et al. 2004; Mu and Zhang 2006; Mu and Jiang 2008a,b; Mu et al. 2015). The results showed that the CNOP could be regarded as representing the optimal

precursors for some events. Wang et al. (2011) found that both CNOP and FSV were able to capture the areas of sensitivity for tropical cyclones at high levels. However, the differences between CNOP and FSV in capturing the weather systems that influence the forecast of typhoon were not examined.

Most previous works on atmospheric predictability and targeted observation using the CNOP method were based on MM5 (Grell et al. 1995) and its tangent linear and adjoint models (Zou et al. 1997). The MM5-CNOP/FSV optimization package was developed by Mu et al. (2007) to study mesoscale predictability and targeted observations, and has since been applied in targeted observation and precursor studies (e.g., Mu et al. 2009; Wang 2009; Qin and Mu 2012; Jiang and Wang 2012). With the WRF Model (Skamarock et al. 2008) gradually replacing MM5, Wang et al. (2011) developed a WRF-based CNOP method and compared it to FSV in two tropical cyclone cases. Since the publication of that work, WRF tangent linear and adjoint models have been redesigned and rewritten (Zhang et al. 2013), and successfully used in forecast sensitivity to observation studies (e.g., Zhang et al. 2014) and the WRF 4DVAR system (Zhang et al. 2015). Readers are referred to Zhang et al. (2013) for details on the WRF tangent linear and adjoint models (called WRFPLUS).

The aim of the work reported in this paper is to build a user-friendly tool that can be used to perform forecast sensitivity to initial perturbation (FSIP) analysis (e.g., identifying variables and/or weather systems that are more important to a given aspect of a forecast, using CNOP and/or FSV) based on a latest version of the WRFPLUS package. The WRF users can apply the FSIP to their own cases through changing certain parameters in a single namelist file. Relative to Wang et al. (2011), this work is unique in the following four aspects: 1) A user-friendly WRF-based FSIP tool was constructed to perform sensitivity analyses with the FSV and CNOP methods using a new version of the WRFPLUS; 2) the FSIP tool was examined and validated by comparing to its MM5 counterpart; 3) the performance of the FSIP tool was assessed not only in a typhoon case in the western North Pacific but also in a winter storm case in the United States; and 4) the sensitivities of the FSIP tool to different optimization windows were examined, revealing a number of differences between the CNOP and FSV methods in their capability to capture the precursors of a weather event.

Section 2 introduces the CNOP and FSV methods, how the FSIP tool was built, and the steps needed to calculate the WRF-based CNOP and FSV, as well as a brief introduction to the two examined cases and the experimental design. The results from the validation of

the FSIP tool in comparison to its MM5 counterpart are presented in section 3. Further applications of the tool to two validation cases for identifying sensitive areas for targeted observations and for detecting important influential weather systems for the forecast total dry energy in the verification area are reported in section 4, followed by a summary and a discussion in section 5. The README file of the namelist and the file structure of the two modules are provided in the appendix.

2. Methodology

a. A brief introduction to the CNOP and FSV methods

The CNOP method involves identifying the initial perturbation that maximizes the forecast difference of a nonlinear system in terms of a chosen forecast metric in a verification area at a verification time. Suppose we have the nonlinear model

$$\begin{cases} \frac{\partial \mathbf{x}}{\partial t} + F(\mathbf{x}) = 0 \\ \mathbf{x}|_{t=0} = \mathbf{x}_0 \end{cases}, \quad (1)$$

where \mathbf{x} is the state vector of the model with an initial value \mathbf{x}_0 , and F is a nonlinear partial differential operator. The solution of Eq. (1) can be expressed in discrete form $\mathbf{x}(t) = M(\mathbf{x}_0)$, where M is the nonlinear propagator and $\mathbf{x}(t)$ is the value of \mathbf{x} at time t .

The cost function $J(\delta \mathbf{x}_0)$ defined in this software is a measure of the difference between perturbed and unperturbed forecasts in the verification area at a chosen time. The CNOP is the initial perturbation that maximizes the chosen J , which satisfies

$$J(\delta \mathbf{x}_0^*) = \max_{\delta \mathbf{x}_0^T C_1 \delta \mathbf{x}_0 \leq \beta} J(\delta \mathbf{x}_0), \quad (2)$$

where

$$J(\delta \mathbf{x}_0) = \{\mathbf{PS}[M(\mathbf{x}_0 + \delta \mathbf{x}_0) - M(\mathbf{x}_0)]\}^T C_2 \{\mathbf{PS}[M(\mathbf{x}_0 + \delta \mathbf{x}_0) - M(\mathbf{x}_0)]\}, \quad (3)$$

and $\delta \mathbf{x}_0^T C_1 \delta \mathbf{x}_0 \leq \beta$ is the constraint that the initial perturbations should satisfy. Here β is specified to make the magnitude of variable perturbations comparable to the analysis errors. The local projection operator \mathbf{P} takes a value of 1 (0) within (outside) the verification area. The linear operator \mathbf{S} maps the variables from model space to the space where the energy norm is calculated. The norm C_1 is used to define the initial perturbations, and C_2 is the norm used to define the cost function $J(\delta \mathbf{x}_0)$.

For simplicity, we let $C_1 = C_2 = C$. In this work, we defined a total dry energy (TDE) norm, which is a component of the total dry energy. The difference between the forecasts with and without the perturbation in a total dry energy norm was defined as TDE':

$$\text{TDE}' = \frac{1}{2} \left[u'^2 + v'^2 + \frac{C_p}{T_r} T'^2 + R_a T_r \left(\frac{P'_s}{P_r} \right)^2 \right], \quad (4)$$

where C_p is the specific heat at constant pressure ($1005.7 \text{ J kg}^{-1} \text{ K}^{-1}$) and R_a is the gas constant of dry air ($287.04 \text{ J kg}^{-1} \text{ K}^{-1}$). The reference temperature and pressure are, respectively, T_r (270 K) and P_r (1000 hPa). Terms u, v, T , and P_s are the zonal and meridional wind components, temperature, and surface pressure, respectively. Here u', v', T' and P'_s are the forecast difference of u, v, T , and P_s , respectively. Many other measures are possible and may be superior for some purposes.

The cost function $J(\delta \mathbf{x}_0)$ was calculated as

$$J(\delta \mathbf{x}_0) = \frac{1}{D} \int_0^1 \int_{D^2} \frac{1}{2} \left(u'^2 + v'^2 + \frac{C_p}{T_r} T'^2 \right) d\eta dD + \frac{1}{D} \int_{D^2} \frac{1}{2} R_a T_r \left(\frac{P'_s}{P_r} \right)^2 dD, \quad (5)$$

where D denotes the verification area and η denotes the vertical coordinate. The left-hand side of $\delta \mathbf{x}_0^T C_1 \delta \mathbf{x}_0 \leq \beta$ is calculated also using Eq. (5) except that D denotes the whole integration domain. To quantify the horizontal and vertical structures of the initial perturbation in terms of the TDE, we calculated the vertical and horizontal integration of TDE', namely, $v\text{TDE}'$ and $h\text{TDE}'$, respectively:

$$v\text{TDE}' = \int_0^1 \frac{1}{2} \left(u'^2 + v'^2 + \frac{C_p}{T_r} T'^2 \right) d\eta + \frac{1}{2} R_a T_r \left(\frac{P'_s}{P_r} \right)^2, \quad (6)$$

$$h\text{TDE}' = \int_D (\text{TDE}') dD, \quad (7)$$

where D denotes a given horizontal integration domain. The surface term was taken into account only for $h\text{TDE}'$ at the surface level. We also examined the horizontal integration of the potential and kinetic energy components ($h\text{PE}'$ and $h\text{KE}'$, respectively),

$$h\text{PE}' = \int_D \frac{1}{2} \left[\frac{C_p}{T_r} T'^2 + R_a T_r \left(\frac{P'_s}{P_r} \right)^2 \right] dD, \quad (8)$$

$$h\text{KE}' = \int_D \frac{1}{2} (u'^2 + v'^2) dD, \quad (9)$$

where only P_s is included for energy calculation at the surface level.

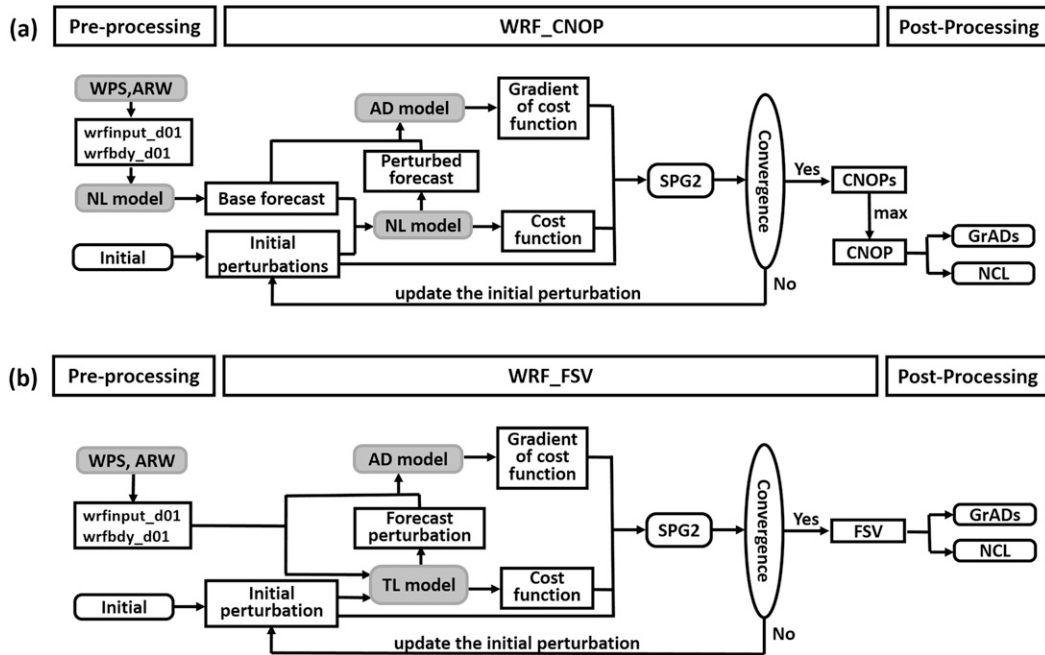


FIG. 1. Flowchart of the FSIP system for the (a) CNOP and (b) FSV methods. Rectangles represent input and output. Ellipsoids represent judgments, rounded rectangles represent modules, shaded and rounded rectangles (WPS, ARW, NL model, TL model, and AD model) are modules from WRF.

The area covered by the grid points with the top 1% largest $vTDE'$ was defined as the sensitive area. It is an area where an analysis error may lead to the largest forecast error in the verification area at the verification time. Thus, assimilating extra observations in this sensitive area may result in the largest decrease in the forecast error of interest.

To find the maximum of the cost function, a particular iteration method that uses forward and adjoint models is usually used. Sometimes, local maxima exist in the cost function defined by Eq. (3). A perturbation associated with a local maximum of J that has a different pattern from a CNOP is then called a local CNOP (Mu and Zhang 2006). Similar to the CNOP, the local CNOP may also have clear physical meaning. For example, the local CNOP was found to represent the optimal precursor of a La Niña event in an ENSO predictability study (Mu et al. 2003; Duan et al. 2004). Local CNOP may not be found or even exist, and there may be more than one.

The FSV method can be regarded as a linear version of the CNOP approach. If the initial perturbation $\delta\mathbf{x}_0$ is sufficiently small and the integration time is not long, then the nonlinear process can be approximately considered as a linear process. In such a case, the cost function is calculated via

$$J(\delta\mathbf{x}_0) = [\mathbf{PSL}(\delta\mathbf{x}_0)]^T C_2 [\mathbf{PSL}(\delta\mathbf{x}_0)], \quad (10)$$

where L is the forward tangent linear propagator of the nonlinear model. The FSV and CNOP calculation

procedures are the same except for the models used for the forward integration in the optimization process. A tangent linear model is used for the FSV calculation, while a nonlinear model is used for the CNOP calculation.

b. Construction of the FSIP tool to produce the CNOP and FSV

A flowchart illustrating the FSIP tool procedure is given in Fig. 1. The FSIP scheme consists of preprocessing, WRF_CNOP/FSV, and postprocessing parts. The stages shown in the shaded boxes are supported by the WRF system. The FSIP tool is designed to be user friendly in its production of the CNOP and FSV. All parameters that need to be set to perform a case study are set in a bash file (CNOP_FSV.sh, a README file for the bash script, and the file structure of the two modules are given in the appendix).

The key to producing the CNOP and FSV is to develop an optimization procedure that solves the constrained initial value problems defined by Eqs. (2), (3), (5), or Eqs. (2), (5), and (10). The conjugate gradient method used in the variational data assimilation system for WRF cannot resolve this constrained optimization problem, and thus the spectral projected gradient 2 (SPG2) minimization algorithm (Birgin et al. 2001; Wang et al. 2011) was adopted to obtain the CNOP and FSV.

The SPG2 optimization algorithm is a method for calculating the minimum value of a function subject to a

constraint using the forward and adjoint versions of the model. Since the CNOP/FSV is the perturbation associated with the maximum cost function, the function for the SPG2 method is defined as the negative cost function in search of a minimum value. For a given first-guess initial perturbation, SPG2 uses the gradient of the above-mentioned cost function to find a further modified initial perturbation such that the cost function decreases the most. This process is iterated until the cost function converges to a minimum value.

The procedures to run the FSIP tool are as follows:

- 1) Set the parameters. The parameters that need to be set include those needed to run the numerical model, such as the integration domain and the physical parameterization schemes, and those needed to calculate sensitive areas, such as the optimization time interval, the value of β , and the verification area. One single domain is used because the tangent linear and adjoint models only work with a single domain in the current version of WRFPLUS. The optimization time (the period between the observation and verification time) is the same as the forecast time in this study. Users also need to specify a verification area where the cost function is calculated. The norm used to constraint the initial perturbation and the cost function is also set here. In this system, total dry energy or parts of it can be used as the norm by changing the parameters.
- 2) Prepare the initial and boundary conditions. The initial and boundary conditions are produced using the WRF preprocessing system (WPS) and the Advanced Research version of WRF Model (ARW). The first-guess initial perturbations can be created randomly or by using the differences in nonlinear forecasts with different lead times but valid at the same time, or the differences between initial fields and nonlinear forecasts, to provide the first-guess field for the SPG2 minimization procedure. In this work, an ensemble of six first-guess initial perturbations (P1–P3 and P1_N–P3_N) is used: P1 represents the differences between initial fields and 24-h nonlinear forecasts; P2 represents the random initial perturbation; P3 represents the mean of P1 and P2; and P1_N–P3_N represent the negative or opposite-signed P1–P3, respectively.
- 3) Produce the CNOP and/or FSV by running the WRF_CNOP and/or WRF_FSV modules shown in Fig. 1. During this iteration process, the SPG2 is executed to calculate FSV and/or CNOP. For FSV, the WRF tangent linear (TL) model is used to estimate the cost function and the adjoint (AD) model is used to provide the gradient. For CNOP, the WRF

nonlinear (NL) model is required to estimate the cost function and the adjoint model is used to produce the gradient as well.

- 4) Postprocessing. Convert the output file data format and plot the CNOP and/or FSV using the Grid Analysis and Display System (GrADs) and the NCAR Command Language (NCL).

The most recent version of WRFPLUS (version 3.6.1; Zhang et al. 2013) was used in this work. The WRFPLUS is a package that contains a full version of the nonlinear WRF Model, its adjoint and tangent linear model versions with limited choices of physical parameterization schemes (Zhang et al. 2013). The nonlinear and adjoint models were used to produce the CNOP, and the tangent linear and adjoint models were used to produce the FSV. Similar to Wang et al. (2011), this work used the nonlinear model and its tangent linear and adjoint models that include only a gravity wave drag parameterization scheme.

c. Cases and experimental design

The FSIP tool was applied in two cases to identify the sensitive region and examine important influential weather systems for the forecast TDE in the verification area. The first case was Typhoon Matsa (2005) in the western North Pacific. Matsa made landfall in south China on 6 August 2005 (Fig. 2a) and caused severe heavy rainfall and flooding in the area indicated by the black box in Fig. 2a. The other case was an intense winter storm off the southeastern coast of the United States, which brought heavy snowfall in the area indicated by the inset in Fig. 2b.

The integration domains for the two cases are shown in Fig. 2. The model used a horizontal resolution of 60 km. The vertical coordinate was divided into 21 levels with the top pressure at 50 hPa. The initial and boundary conditions were provided by the NCEP Final Analysis (NCEP FNL) data at $1^\circ \times 1^\circ$ and 6-h intervals.

In the control experiment for Typhoon Matsa, 0000 UTC 5 August was set as the initial time and 0000 UTC 6 August, which was 24 h after the initial time, was set as the verification time (Table 1). For the winter storm, 0000 UTC 24 January 2000 was set as the initial time and the time 24 h after the initial time was the verification time. The verification area covered the location of the typhoon center (the black box in Fig. 2a) and the heavy snowfall (the inset in Fig. 2b).

3. Validation of the FSIP

Considering that the CNOP/FSV was initially developed based on MM5 and that the MM5-based

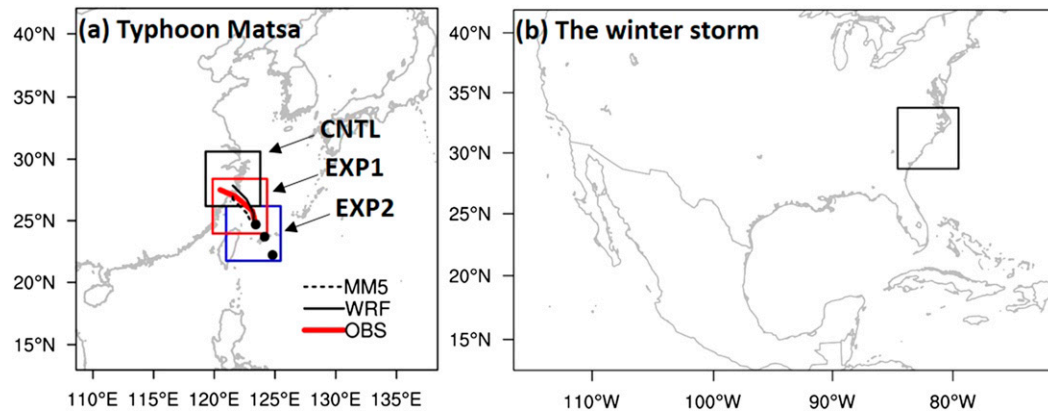


FIG. 2. The integration domain of the model and the verification areas (insets) for (a) Typhoon Matsa, and (b) the winter storm case. The best track from the Japan Meteorological Agency (red) and the simulated track (black) of Typhoon Matsa in WRF (black solid) and MM5 (black dotted) for the control experiment are also shown in (a). The black dots in (a) represent the typhoon center at the initial time of the control experiment, EXP1, and EXP2.

CNOP/FSV has been applied in many targeted observation and predictability studies (e.g., Mu et al. 2007, 2009; Wang 2009; Qin and Mu 2012; Jiang and Wang 2012), we examined whether the generation of the final initial perturbations in the WRF-based CNOP/FSV system developed in the present study was generally consistent with the MM5-based CNOP/FSV to ensure the system worked as expected when applied in the case of Typhoon Matsa, as an example.

The MM5-CNOP/FSV were calculated using MM5 and its tangent linear and adjoint models. Both the MM5 and WRF systems used exactly the same configuration except for the different dynamical core and planetary boundary layer (PBL) scheme. MM5 used a bulk PBL, while WRF used the surface drag.

The cost functions in both models increased rapidly and achieved a maximum after about 15 iterations. Similar to the MM5-FSV/CNOP, the FSIP tool also had a local CNOP in addition to the CNOP. The detection of the CNOP and local CNOP is demonstrated in Figs. 3–5. As shown in Fig. 3a, the cost functions of six first-guess initial perturbations for the CNOP and local CNOP calculations converged into two apparently different ranges of magnitude (three in 42 417–42 420 in black and three in 39 394–39 398 in red). The converged J maximum was independent of the choice of first-guess initial perturbations. The initial perturbations produced after all the iterations had quite similar patterns within

one range but a significant difference was observed between the two ranges in terms of the distribution of the sensitive area [Figs. 4a(1) and 4a(2) vs Figs. 4a(3) and 4a(4), in which the initial perturbations corresponding to the J maximum and J minimum of the two ranges were shown], the final initial perturbations at a certain level [Figs. 4b(1) and b(2) vs Figs. 4b(3) and 4b(4)], and the $hTDE'$, hKE' , and hPE' [integrated over the whole domain; Figs. 4c(1) and 4c(2) vs Figs. 4c(3) and 4c(4)]. The

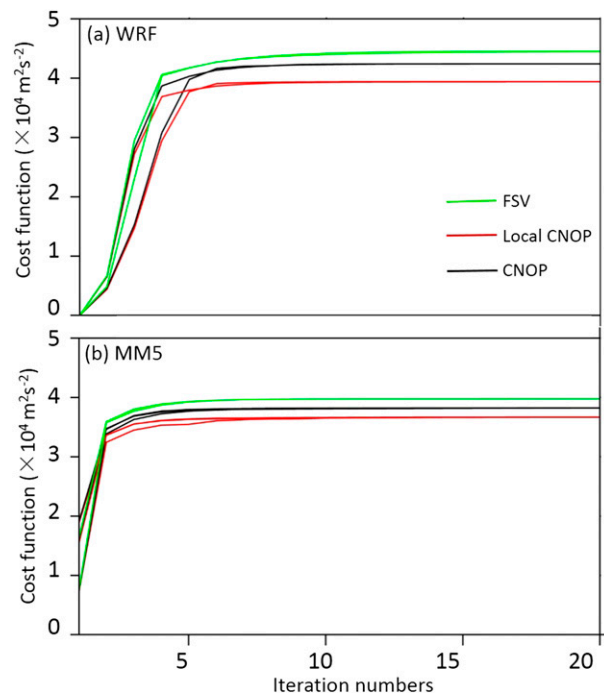


FIG. 3. Variation of the cost function with the number of iterations for Typhoon Matsa, with the CNOP in black, the local CNOP in red, and the FSV in green, based on (a) WRF and (b) MM5.

TABLE 1. Initial and verification times for Typhoon Matsa.

Expt name	Initial time	Verification time
Control	0000 UTC 5 Aug 2005	0000 UTC 6 Aug 2005
EXP1	1200 UTC 4 Aug 2005	1200 UTC 5 Aug 2005
EXP2	0000 UTC 4 Aug 2005	0000 UTC 5 Aug 2005

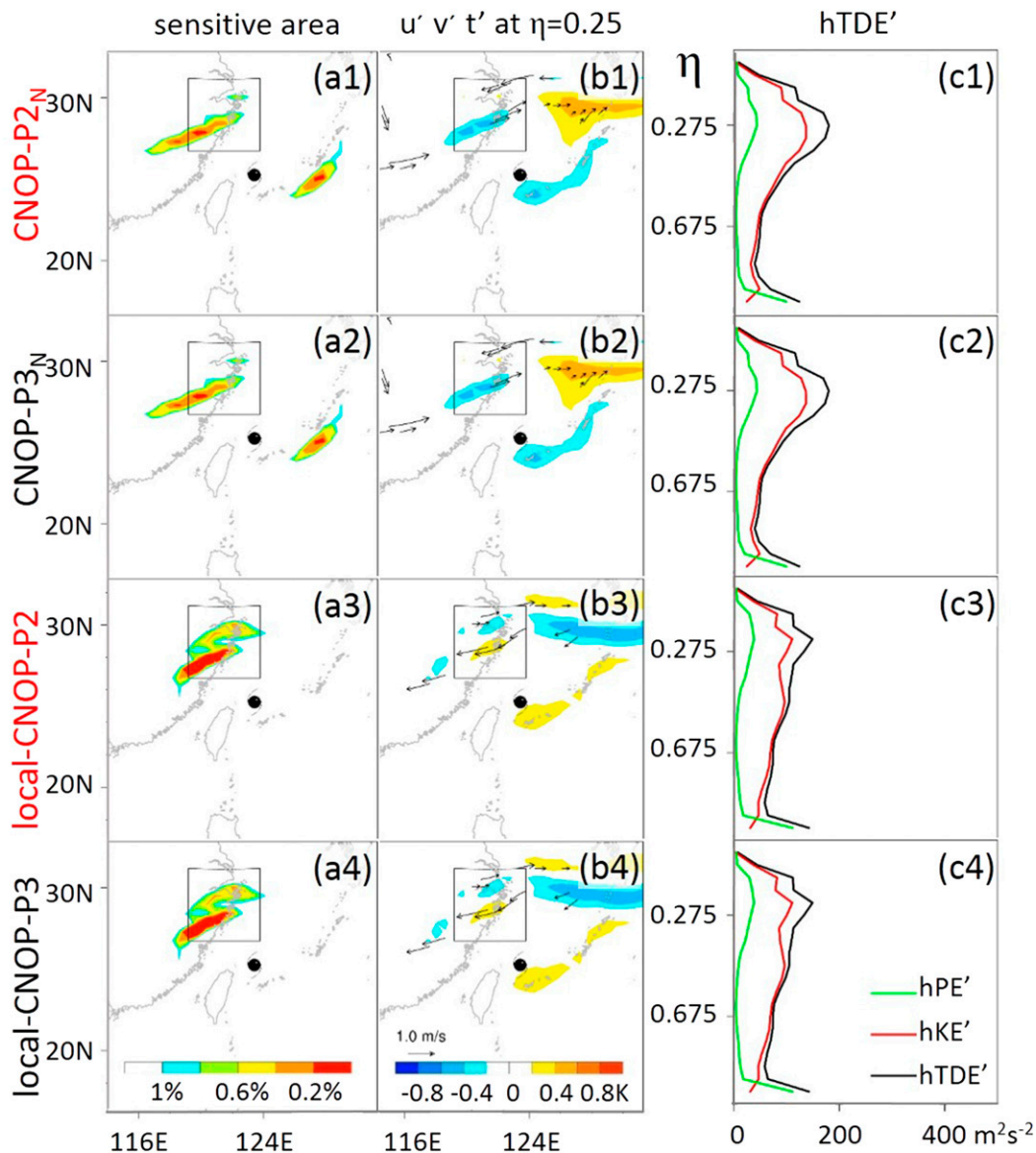


FIG. 4. The (a) sensitive area (shaded), (b) horizontal distributions of wind (arrows, m s^{-1}) and temperature (shaded, K) perturbations at the $\eta = 0.25$ level (about 300 hPa), and (c) vertical distributions of $hTDE'$, hKE' , and hPE' ($\text{m}^2 \text{s}^{-2}$, integrated over the whole domain) identified by the CNOP group (upper two rows) and the local CNOP group (lower two rows) in WRF for Typhoon Matsa. The inset denotes the verification area. The typhoon symbol represents the typhoon center at the initial time. P2, P3, P2_N, and P3_N represent the results from experiments with the first-guess initial perturbations that produce the maximum and minimum cost functions in both the CNOP and local CNOP ranges. The row labels on the left of the CNOP and local CNOP are marked in red.

CNOP was the final initial perturbation corresponding to the largest J maximum in the range with the larger J maxima [42 420; Figs. 4a(1), 4b(1), and 4c(1)], while the local CNOP was the final initial perturbation corresponding to the largest J maximum in the range with the smaller J maxima (32 398; Figs. 4a(3), 4b(3), and 4c(3)). These features were quite similar to their MM5 counterparts (Figs. 3b and 5).

The sensitive areas of the CNOP and local CNOP methods identified using the two models were generally similar in terms of their location and shape of $\nu TDE'$ and perturbation distributions at $\eta = 0.25$ (~ 300 hPa) though there were differences in some of the details [Figs. 4a(1) and 4b(1) vs Figs. 5a(1) and 5b(1); Figs. 4a(3) and 4b(3) vs Figs. 5a(3) and 5b(3)]. Both identified a sensitive area to the northwest of the typhoon

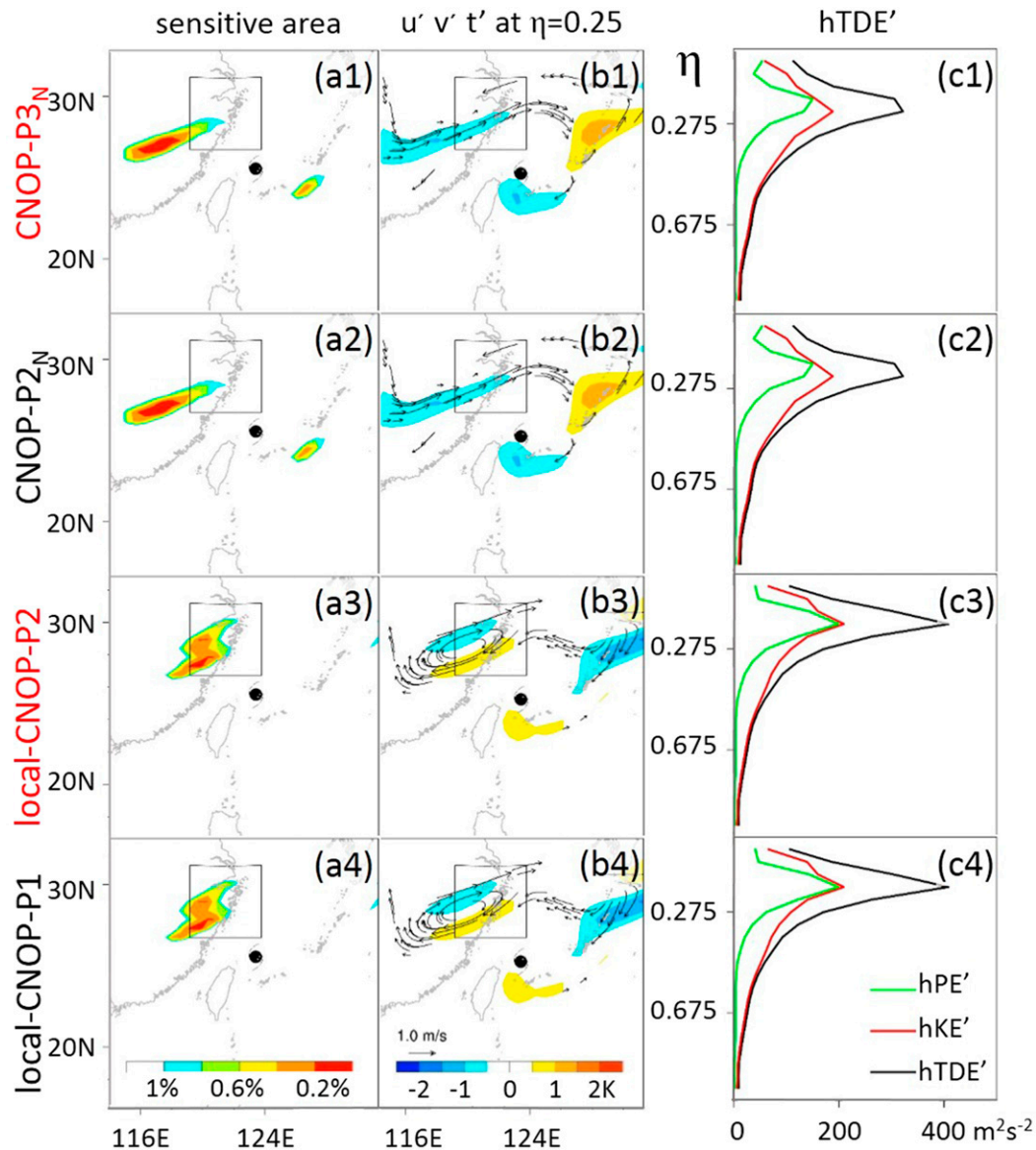


FIG. 5. As in Fig. 4, but using MM5. P1, P2, P2_N, and P3_N represent the results from experiments with the first-guess initial perturbations that produce the maximum and minimum cost functions in both the CNOP and local CNOP ranges.

center, but the WRF sensitive area was located more to the northeast. Furthermore, both models showed that the energy all peaked at the upper levels, but with some differences in the details of the vertical distribution, such as the magnitude, and the relative contributions from the kinetic and potential energy [Fig. 4c(1) vs Fig. 5c(1); Fig. 4c(3) vs Fig. 5c(3)]. The WRF Model showed a larger hTDE' near the surface than that of MM5 likely because of different PBL schemes. The evolution of the sensitive area produced by the CNOP and local CNOP methods with the number of iterations was also similar between the two models (Figs. 6a and 6b for WRF; Figs. 6c and 6d for

MM5). The results showed that the morphology of the sensitive areas became stable after about 15 iterations (Fig. 6). The difference between the locations of the CNOP and local CNOP sensitive areas was apparent after about five iterations, and it became larger with the increase of iteration number in both models (Fig. 6). The same was true for the evolution of the sensitive area of the FSV method (figures not shown). More details on the detection of the sensitive area will be discussed in section 4a.

Different from two converged maxima of J in the non-linear model, J converged into a single maximum in the linear model used to produce the FSV in both WRF and

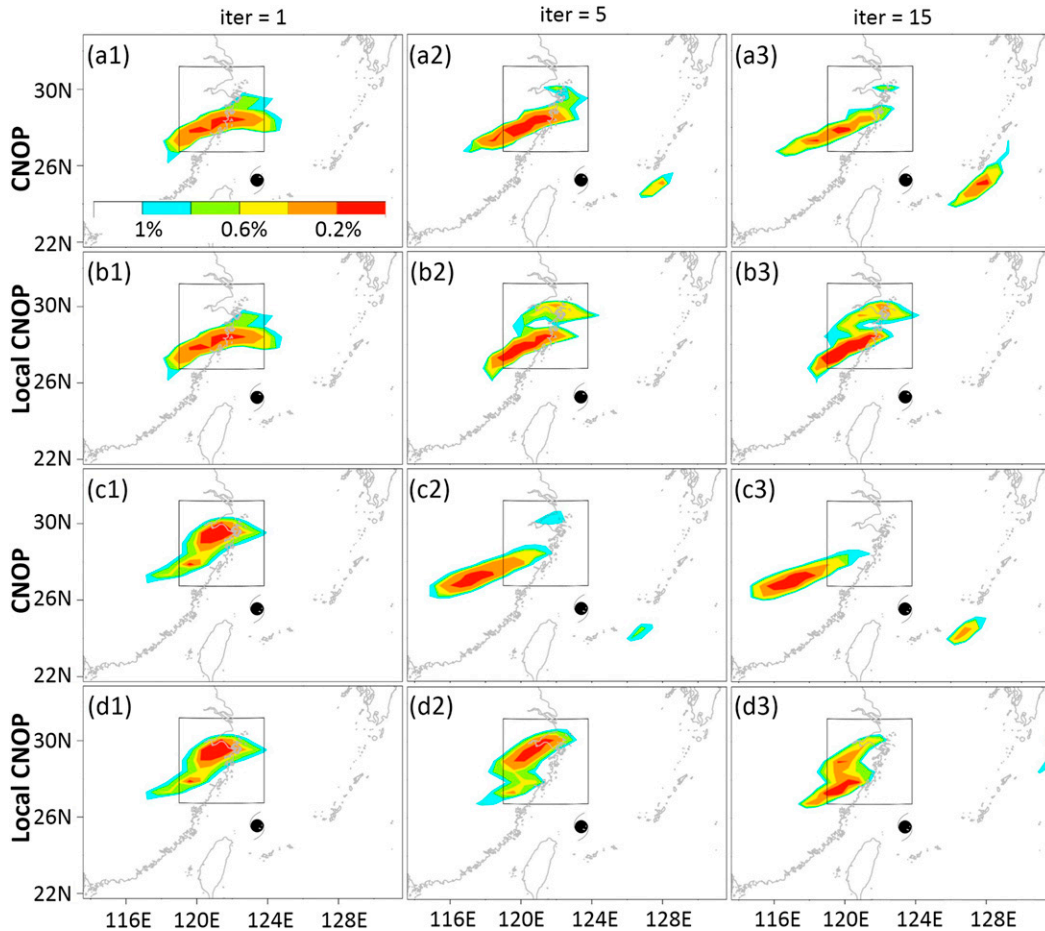


FIG. 6. Development of sensitive areas with the number of iterations (given at the top of each column) in the (a),(c) CNOP and (b),(d) local CNOP using (a),(b) WRF and (c),(d) MM5 for Typhoon Matsa. The inset denotes the verification area. The typhoon symbol represents the typhoon center at the initial time.

MM5 (Fig. 3). The sign of the FSV, however, is arbitrary. The results of both models showed that an opposite-signed first-guess initial perturbations produced opposite-signed FSVs [Figs. 7b(1) vs 7b(2) and Figs. 7b(3) vs 7b(4), in which the initial perturbations corresponding to the first-guess initial perturbations that had opposite signs were shown]. To fully investigate the nonlinear evolution of the FSV, we performed two nonlinear runs using opposite-signed FSVs and used the one that had the maximum J as the final FSV. The results showed that the distribution of the sensitive area, the perturbation at a certain level, and the $hTDE'$, hKE' , and hPE' (integrated over the whole domain) were all quite similar between the two models with the differences similar to those in the CNOP and local CNOP.

4. Application of the FSIP tool

This section demonstrates that the FSIP was a potentially useful tool in identifying the sensitive region for

targeted observation and detecting important influential weather systems for the norm TDE' in the verification area at the forecast time for both the typhoon and winter storm cases.

a. Identification of the sensitive region for targeted observation

For targeted observation, a key step is to specify the sensitive region where additional observations are collected, which will potentially have the largest impact on forecasts over a verification region for a given forecast metric. The questions that need to be answered are not only where to collect the observations but also what types of observations will be most beneficial. This question can be addressed by comparing the contributions of different variables to the final forecast error and their vertical distributions.

The sensitive area was determined based on the distribution of the final initial perturbation and its impact on the J in this study. Thus, we needed first to examine

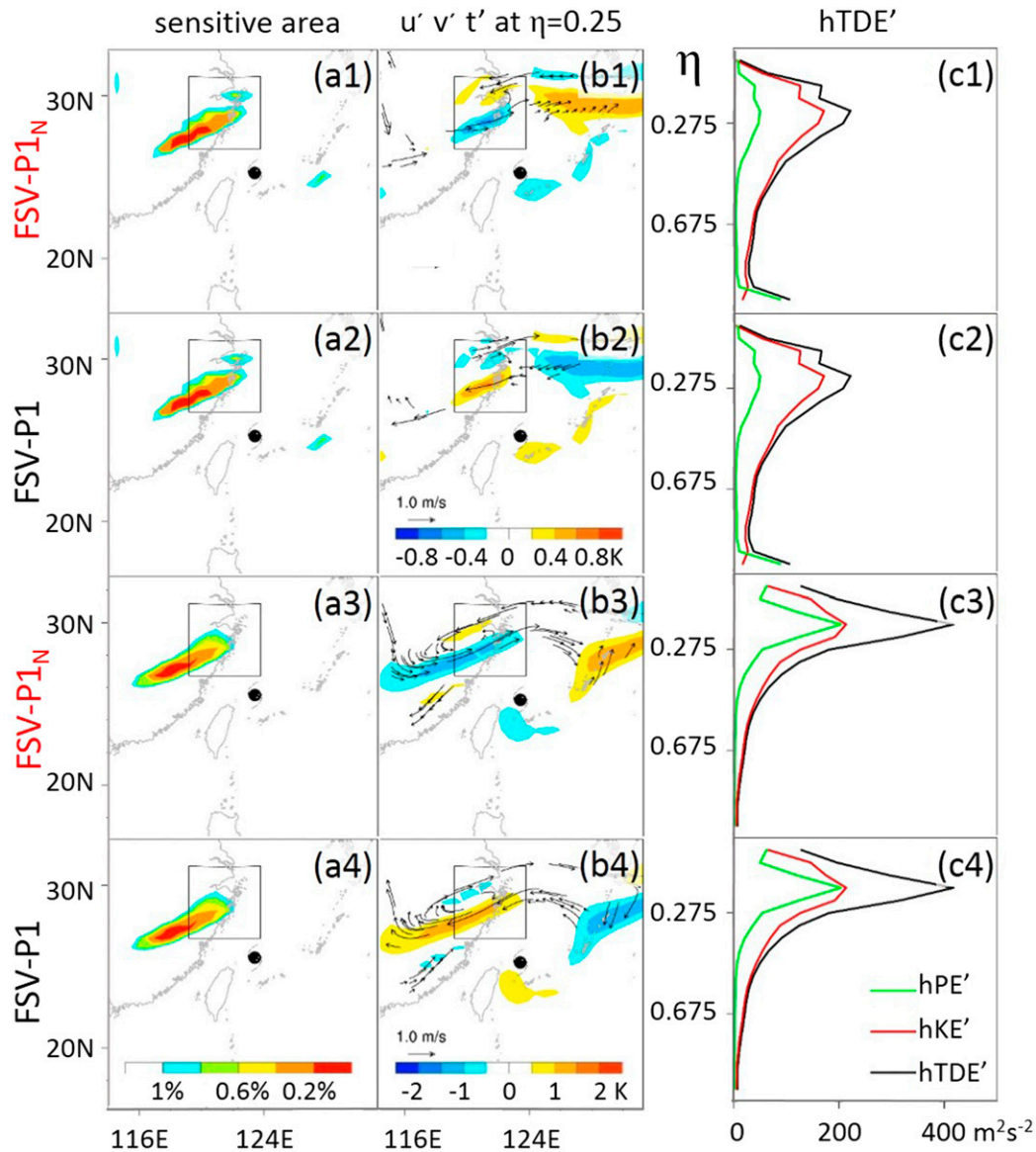


FIG. 7. The (a) sensitive area (shaded), (b) horizontal distributions of wind (arrows, m s^{-1}) and temperature (shaded, K) perturbations at the $\eta = 0.25$ level (about 300 hPa), and (c) vertical distributions of $hTDE'$, hKE' and hPE' ($\text{m}^2 \text{s}^{-2}$, integrated over the whole domain) identified by the FSV method in WRF (upper two rows) and MM5 (lower two rows) for Typhoon Matsa. The inset denotes the verification area. The typhoon symbol represents the typhoon center at the initial time. P1 and P1_N represent the results from experiments with different first-guess initial perturbations.

whether the final initial perturbations evolved into the verification area at the verification time. The influence of the three final or optimized initial perturbations (the CNOP, local CNOP, and FSV) on the nonlinear forecast was investigated by computing the difference between two WRF simulations—one with, and one without, the optimal perturbations in the whole domain.

For Typhoon Matsa, the $vTDE'$ of all three perturbations evolved into the verification area after 24 h of development [Figs. 8a(1)–a(3)] with the CNOP

producing larger $vTDE'$ integrated over the verification area at the verification time than local CNOP and FSV (Fig. 9a). The larger magnitude of $vTDE'$ in the CNOP and local CNOP than that in the FSV was probably because that the CNOP-type methods fully take into account the nonlinear propagation operator. A comparison between the vertical distributions of $hTDE'$ at the initial and verification times showed that the perturbation growth mainly occurred at upper levels. This was related to a more efficient propagation

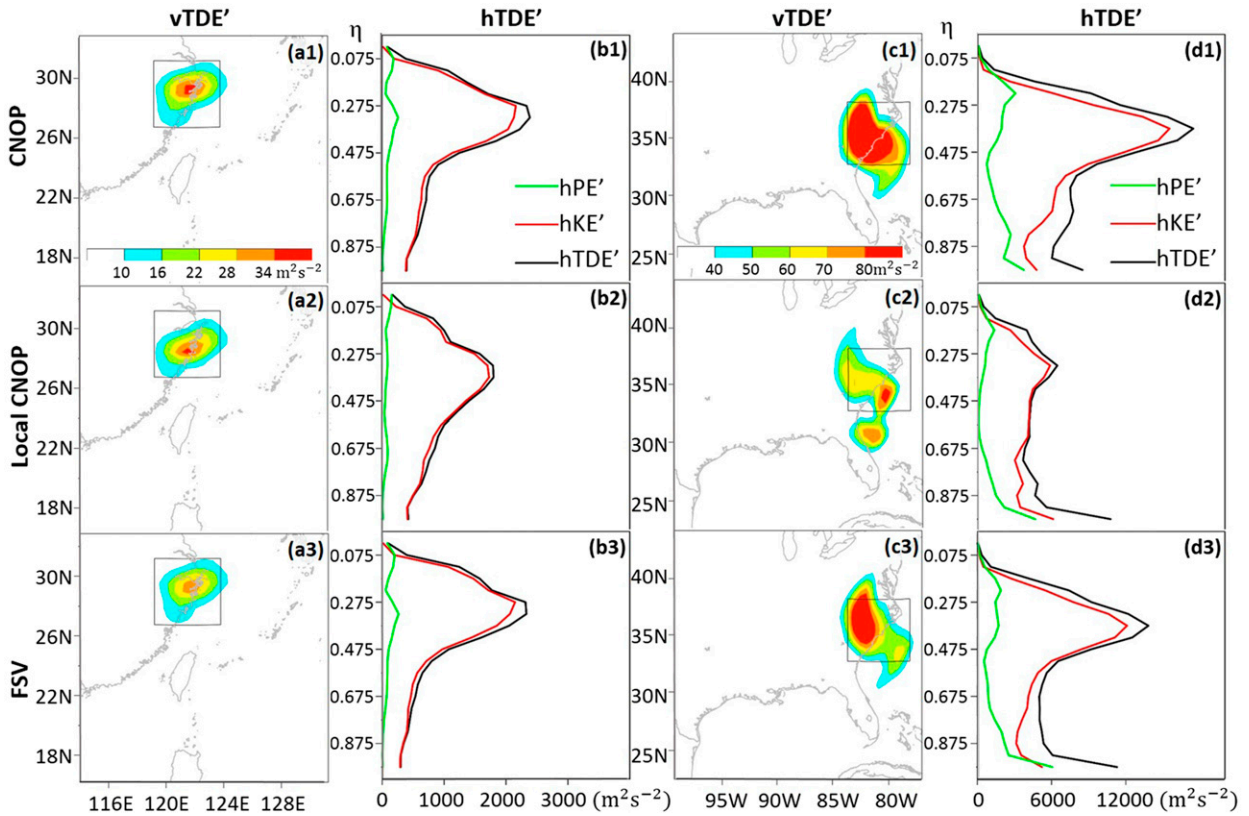


FIG. 8. [a(1)–a(3)] The horizontal distribution of $vTDE'$ (shaded, $m^2 s^{-2}$) and the corresponding vertical distribution of $hTDE'$, hKE' , and hPE' ($m^2 s^{-2}$) integrated over the verification area after a 24-h nonlinear integration by adding the [a(1),b(1)] CNOP, [a(2),b(2)] local CNOP, and [a(3),b(3)] FSV for Typhoon Matsa. The inset in (a) denotes the verification area. (c),(d) As in (a) and (b), but for the winter storm case.

of information at high altitudes. The most notable increase in the forecast difference was contributed mainly by the kinetic energy in all three perturbations [Figs. 8b(1)–b(3) vs Figs. 4c(1), 4c(3), and 7c(1)]. This result indicates that wind observations might be more important than temperature observations for the Matsa case.

The sensitive area for targeted observation was determined as a localized area where the $vTDE'$ was the largest at the observation time because of limited observation resources. As given in section 2a, the area covered by the top 1% of grid points with the largest $vTDE'$ was defined as the sensitive area in this work. To investigate the effect of the extents of the perturbations on the forecast norm, the impact of perturbing the whole domain was compared to that of perturbing just the sensitive region. To make a fair comparison between the three methods and to reveal the relative importance of the locations of their sensitive areas, the perturbations were normalized with respect to the maximum $vTDE'$ in the sensitive area of all three perturbations (referred to as max_vTDE'). Specifically, the perturbations in the sensitive area of one method were multiplied by a number so that the maximum $vTDE'$ of this method was equal to

the max_vTDE' . Figure 9c shows that if only the normalized perturbations in the sensitive area were added to the initial fields, that the $vTDE'$ integrated over the verification area of all three perturbations still grew rapidly with time, with the CNOP producing the largest value at the verification time. The localized initial perturbation also propagated into the verification area and produced a large energy difference there [Figs. 10a(1)–a(3)], demonstrating the validation of the identified sensitive area. The sensitive areas identified by the three methods were generally similar with a banded area to the northwest of the typhoon center [Figs. 4a(1), 4a(3), and 7a(1)]. The CNOP and FSV methods were more similar in both location and pattern of the sensitive areas [Figs. 4a(1) and 7a(1)]. They both identified two sensitive areas: one to the northwest of the typhoon center and one to the east of the typhoon center. The $hTDE'$ of all three initial perturbations peaked at upper levels, with the magnitude of hPE' smaller than that of hKE' [Figs. 4c(1) and 7c(1)]. Similar features were observed in the vertical distribution of $hTDE'$, hPE' , and hKE' if only the normalized perturbation in the sensitive area were added [Figs. 10b(1)–b(3)].

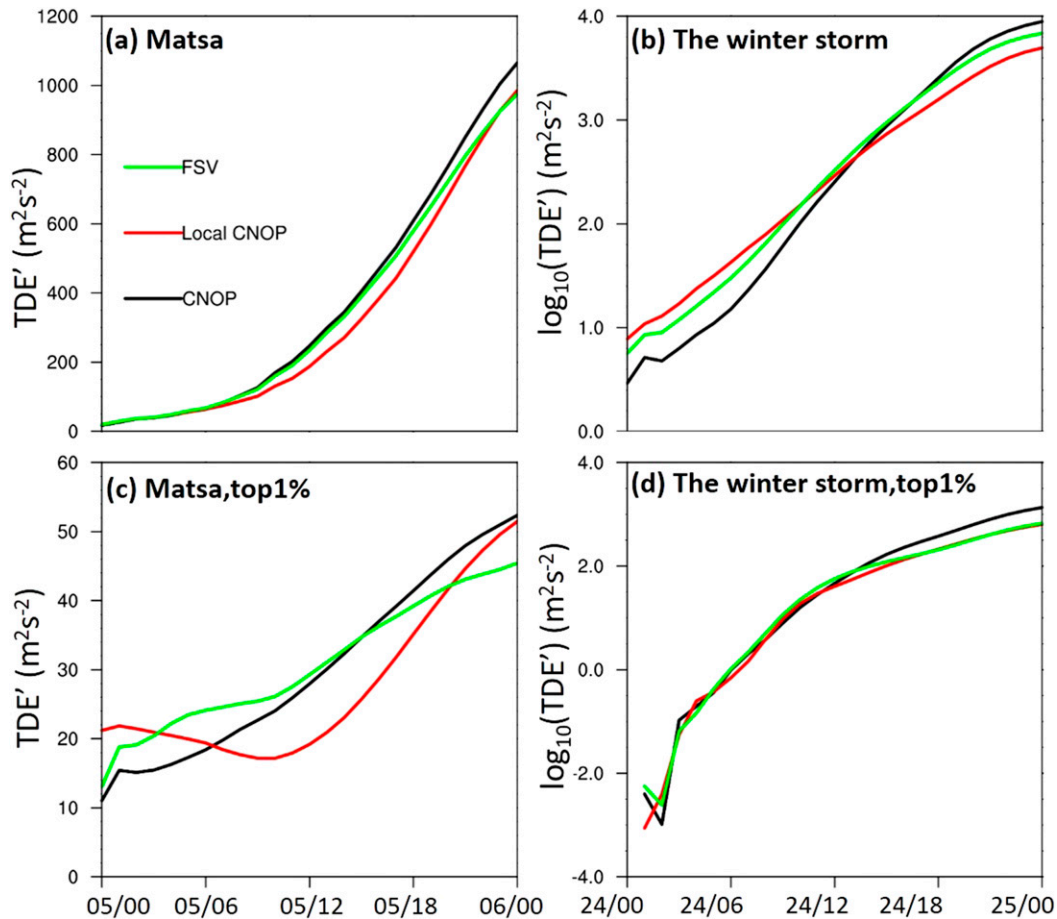


FIG. 9. The nonlinear evolution of TDE' integrated over the verification area and all vertical levels during the optimization time period for Typhoon Matsa by adding (a) the perturbations in the whole domain and (c) the normalized perturbations just in the sensitive area. (b),(d) As in (a) and (c), but for the winter storm case.

Besides the typhoon case, the FSIP tool was also applied in the winter storm case (Fig. 11). The location and shape of the sensitive areas identified by the CNOP and FSV methods were also similar to each other in the winter case (Figs. 11a and 11c). Their vertical distribution of the $hTDE'$ all peaked in the middle levels (Figs. 11g and 11i). The local CNOP method had sensitive areas at similar locations to those of the CNOP and FSV methods but with a more scattered distribution (Fig. 11b) and a vertical distribution of energy peaking at lower levels (Fig. 11h). An apparent difference between the typhoon case and the winter storm case was that the potential energy was significantly larger than the kinetic energy in the winter case (Figs. 11g–i), while the potential energy was much smaller than the kinetic energy in the typhoon case (Figs. 4c(1), 4c(3), and 7c(1)). Though different in the initial distribution, all three final initial perturbations evolved into the verification area [Figs. 8c(1)–c(3)] and peaked at upper levels after 24 h of evolution [Figs.

8d(1)–d(3)], and were mainly contributed by the kinetic energy, indicating the growth of the perturbation was mainly contributed from kinetic energy at upper levels, similar to what occurred in the typhoon case. This result indicates that wind observations might be more important than temperature observations also for the winter storm case. An apparently larger energy difference of the CNOP than that of local CNOP and FSV was also found in the winter storm case [Figs. 8c(1)–c(3), 8d(1)–d(3), and 9b]. Similar features were also observed if only the normalized perturbations in the sensitive area were added to the initial fields (Figs. 9d, 10c, and 10d).

Although the localized sensitivity regions that were determined using the top 1% of grid points with the largest $vTDE'$ can be sampled in practice, these localized regions were only part of the broad signal given by the whole perturbations [Figs. 4b(1) and 7b(1)] and thus may not be always effective. The limited coverage of targeted observations could be one of the main reasons why a neutral

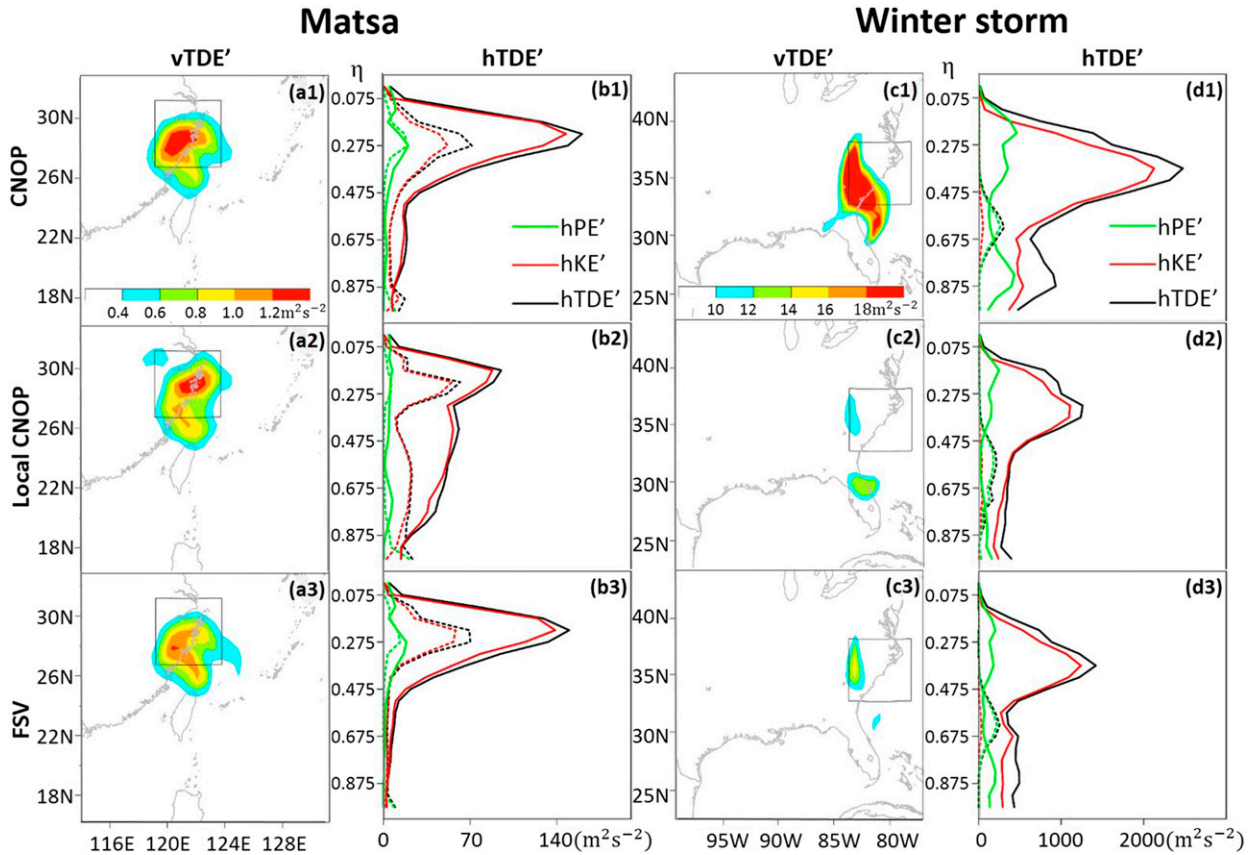


FIG. 10. [a(1)–a(3)] The horizontal distribution of $vTDE'$ (shaded, $m^2 s^{-2}$) at the verification time and the corresponding vertical distribution of $hTDE'$, hKE' , and hPE' ($m^2 s^{-2}$) integrated over the sensitive area at the observation time (dotted) and integrated over the verification area after 24-h nonlinear integration (solid) by adding the normalized [a(1),b(1)] CNOP, [a(2),b(2)] local CNOP, and [a(3),b(3)] FSV only in the sensitive area for Typhoon Matsa. The inset in (a) denotes the verification area. (c),(d) As in (a) and (b), but for the winter storm case.

impact on observations from global hawks on winter storm forecasts was obtained (Hamill et al. 2013).

b. Detection of important influential weather systems for a given forecast metric

The evolution of TDE' at a particular level during the whole optimization time by adding the final initial perturbation over the whole domain was examined to detect the important influential weather systems for the forecast TDE in the verification area. For Typhoon Matsa, the TDE' evolution of the CNOP at 200 hPa was examined every 12 h (Figs. 12a–c). There were three regions of high sensitivity at 200 hPa: One was located between the typhoon center and the midlatitude trough (B in Fig. 12a); another appeared between the typhoon center and the subtropical high (C in Fig. 12a); and a third was situated along the midlatitude trough (A in Fig. 12a). Following the integration, the regions of high sensitivity gradually propagated into the verification area, indicating that the trough and subtropical high may

have had an important influence on the TDE' in the verification area, or the structure of Matsa, at the verification time.

A similar conclusion was obtained in the winter storm case (Figs. 12d–f). The TDE' of CNOP at 500 hPa showed that a region of high sensitivity surrounded the trough axis. With the integration, the regions of high sensitivity propagated along with the trough axis and finally into the verification area. This result indicates the likely important influence of the trough on the TDE' in the verification area at the verification time.

The TDE' of the local CNOP and FSV also showed similar characteristics (figures not shown). Typhoon Matsa was also studied in Wang et al. (2011). Though the detailed structures of the CNOP, local CNOP, and FSV were different from this work, they also found that the regions of high sensitivity at upper levels were associated with the midlatitude trough and subtropical high.

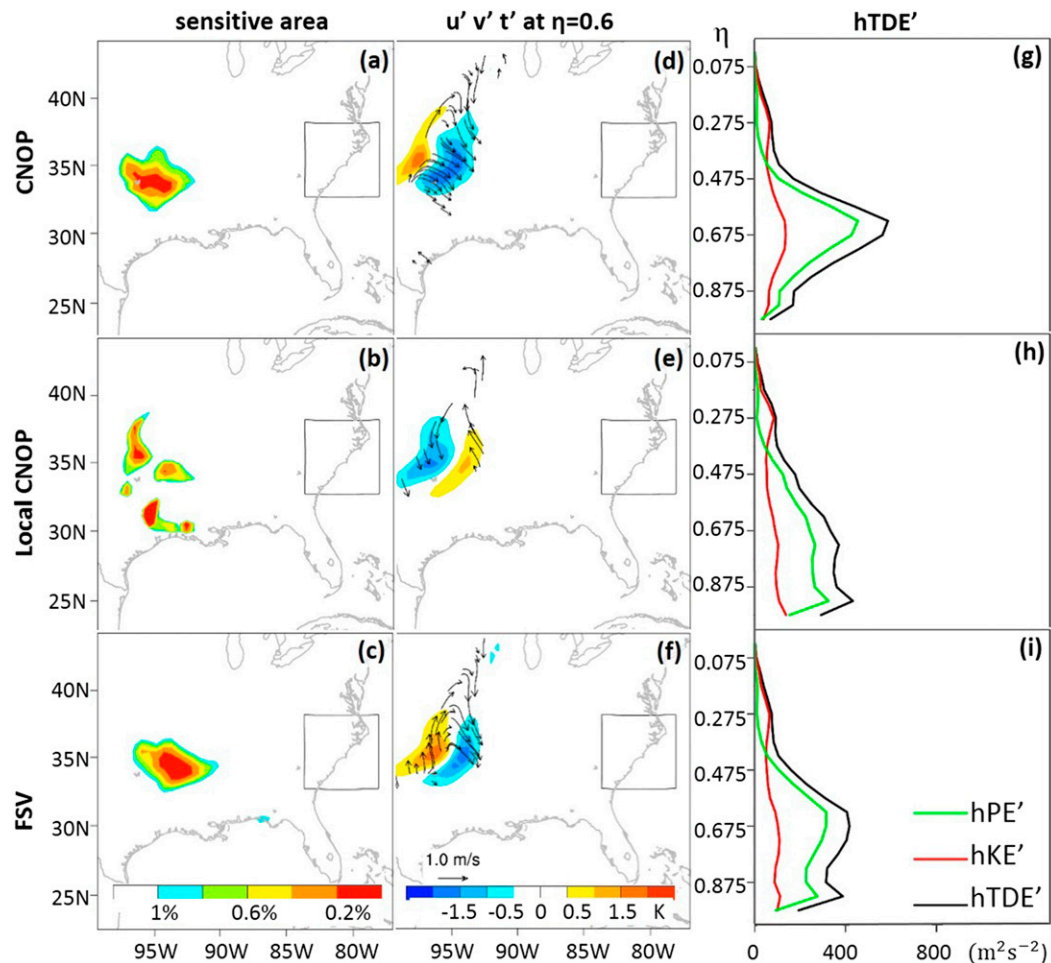


FIG. 11. (first column) The sensitive area (shaded), (second column) the horizontal distributions of wind (arrows; $m s^{-1}$) and temperature (shaded; K) perturbations at $\eta = 0.6$ level (about 600 hPa), and (third column) the vertical distributions of hTDE', hKE', and hPE' ($m^2 s^{-2}$; integrated over the whole domain) identified by the (first row) CNOP, (second row) local CNOP, and (third row) FSV in WRF for the winter storm case. The inset denotes the verification area.

Sensitivity experiments were then conducted to investigate the capability of CNOP, local CNOP, and FSV in detecting important influential weather systems for the forecast TDE in the verification area with Typhoon Matsa used as an example. Experiment 1 (EXP1) and EXP2 (Table 1) were performed in the same way as the control experiment except that the CNOP and FSV were calculated using different observation times at 1200 UTC 4 August and 0000 UTC 4 August, respectively, which were 12 and 24 h earlier than the control experiment. The verification times for the two experiments were 24 h after their initial times. Their verification areas are denoted by the red and blue boxes, respectively, in Fig. 2a.

In EXP1, the sensitive areas identified with the three perturbations differed greatly [Figs. 13a(1)–a(3)]. The CNOP method identified a sensitivity area

to the east of the typhoon center, the local CNOP method identified a sensitivity area to the north-northwest of the typhoon center, and the FSV method identified a sensitivity area to its northwest. The CNOP and local CNOP peaked at both upper and lower levels, while the FSV peaked only at lower levels [Figs. 13b(1)–b(3)]. In EXP2, when the observing time was 12 h earlier than in EXP1, sensitivity areas identified with the CNOP method were mainly located to the south, east, and north of the typhoon center [Fig. 13c(1)], while the local CNOP method identified sensitivity areas to the east and north of the typhoon center [Fig. 13c(2)], and the FSV method identified sensitivity areas to the east of the typhoon center [Fig. 13c(3)]. The sensitivity areas identified by all three perturbation methods became closer to the typhoon center, although they were not

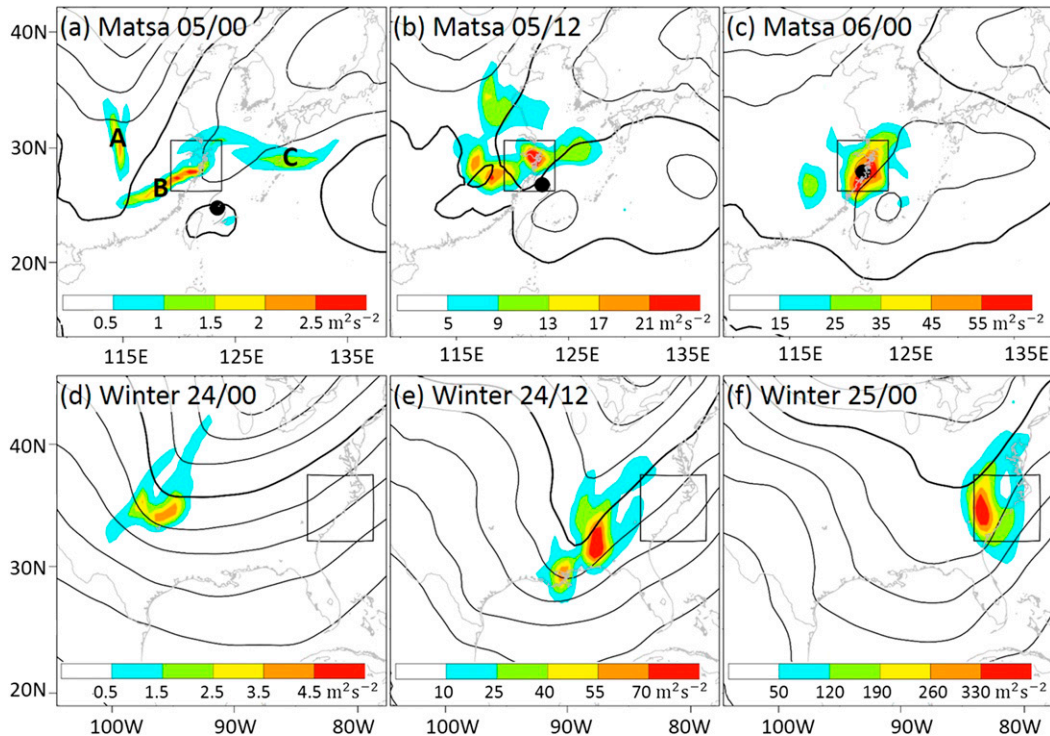


FIG. 12. Geopotential height (contour; m) and the TDE' (shaded; $m^2 s^{-2}$) at (a)–(c) 200 hPa for Typhoon Matsa and (d)–(f) 500 hPa for the winter storm case during the 24-h nonlinear integration of the CNOP at (a),(d) the initial time, (b),(e) 12 h, and (c),(f) 24 h into the integration. The inset represents the verification area. The typhoon symbol represents the typhoon center at the respective forecast times in the nonlinear simulation without perturbation.

identical. The energy all peaked at the upper levels [Figs. 13d(1)–d(3)].

Considering that most perturbations peaked at upper levels, the regions of high sensitivity at high levels were used to examine the physical meaning of the sensitive area. The horizontal distribution of TDE' at 200 hPa is shown in Fig. 14 for both EXP1 and EXP2, as well as the results of the control experiment. In the control experiment, all three perturbation methods identified regions of high sensitivity associated with the subtropical high and midlatitude trough (Figs. 14a–c). In EXP1, the local CNOP method identified regions of high sensitivity associated with the subtropical high, while the CNOP and FSV methods identified only regions of high sensitivity close to the typhoon itself (Figs. 14d–f). In EXP2, the regions of high sensitivity identified by all three perturbation methods were mainly located close to the typhoon center (Figs. 14g–i), indicating that the structure of the typhoon (in terms of TDE') in the verification area at the verification time was the most sensitive to the TC structure itself at this observation time.

A comparison among the three experiments showed that the evolution of the sensitive area with time did

reveal the important weather systems that affected the typhoon. All three perturbation methods captured similar sensitive regions while the typhoon was quite close to or far away from the midlatitude trough and subtropical high. When the distance between the typhoon center and other systems was neither too far nor too close, the identified regions of sensitivity differed greatly. The local CNOP method had better capability than the CNOP and FSV methods of capturing important influential weather systems for the forecast TDE in the verification area.

5. Summary and discussion

In this study, a user-friendly WRF-based FSIP tool was developed to obtain the CNOP or FSV for examining the forecast sensitivity to the initial perturbation. This tool can be used to conduct sensitivity analysis, to identify sensitive regions for targeted observation, and to investigate important influential weather systems for the forecast TDE in the verification area at the verification time.

The performance of the FSIP tool was tested with Typhoon Matsa (2005) in the western North Pacific

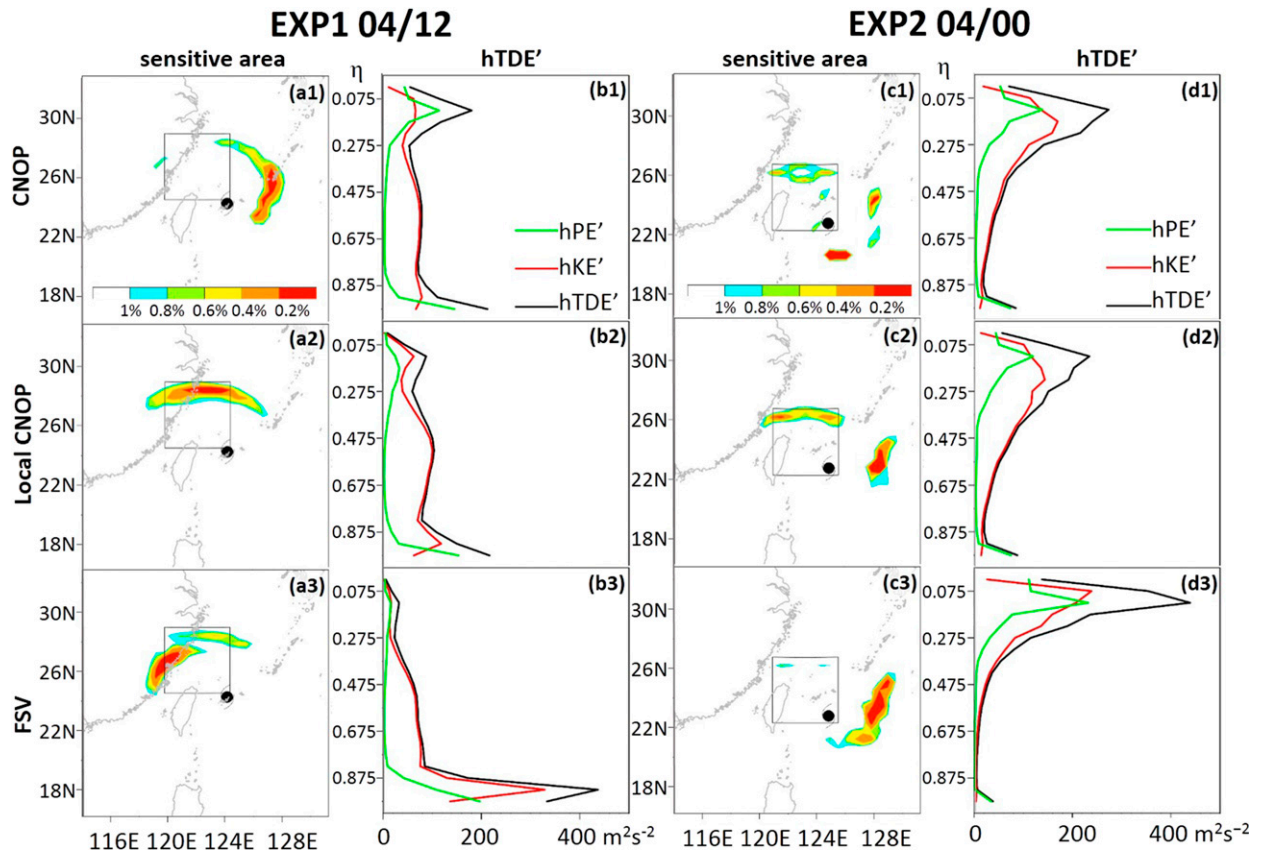


FIG. 13. The [a(1)–a(3)] sensitive area (shaded) and [b(1)–b(3)] vertical distribution of hTDE', hKE', and hPE' ($\text{m}^2 \text{s}^{-2}$; integrated over the whole domain) identified by the [a(1),b(1)] CNOP, [a(2),b(2)] local CNOP, and [a(3),b(3)] FSV methods for EXP1, which was initialized at 1200 UTC 4 Aug. The inset denotes the verification area. The typhoon symbol represents the typhoon center at the initial time. (c),(d) As in (a) and (b), but for EXP2, which was initialized at 0000 UTC 4 Aug.

and compared with the MM5-based CNOP and FSV systems. In general, the sensitive areas identified with the two models were similar in terms of both the location and pattern. The differences lay mainly in the identification of different minor sensitive areas and the magnitude of the three types of energy at different levels as well as the different contributions from the potential and kinetic energy. More cases were tested and the results further supported the conclusion. Thus, the knowledge obtained with the previous MM5-based CNOP/FSV generally applies in the WRF-based FSIP tool.

The FSIP tool was then examined to show its capability in identifying sensitive regions for targeted observation and investigating important influential weather systems for the forecast TDE in the verification area for Typhoon Matsa (2005) and a winter storm case in the United States in 2000. The results showed that the WRF-based CNOP, local CNOP and FSV methods were quite similar in terms of the location and pattern of the identified sensitive area for both Typhoon Matsa and

the winter storm case. A major difference was in the identification of different minor sensitive areas and the magnitude of the three types of energy in the vertical direction. The forecast energy differences using the three types of initial perturbations at the forecast time all peaked at the upper levels and were mainly contributed by kinetic energy. The three types of initial perturbations showed that the wind observations might be more important than temperature observations for both Typhoon Matsa and the winter storm case. The impact of the CNOP on the forecast in the verification area was apparently larger than that of the local CNOP and FSV.

The three perturbations were all able to capture important influential weather systems for the forecast TDE in the verification area. The evolution of perturbations at upper levels for the typhoon case showed that the forecast energy metric was quite sensitive to the trough and subtropical high. In the winter storm case, the evolution of perturbations at middle levels showed the sensitivity of the forecast energy metric to the trough in

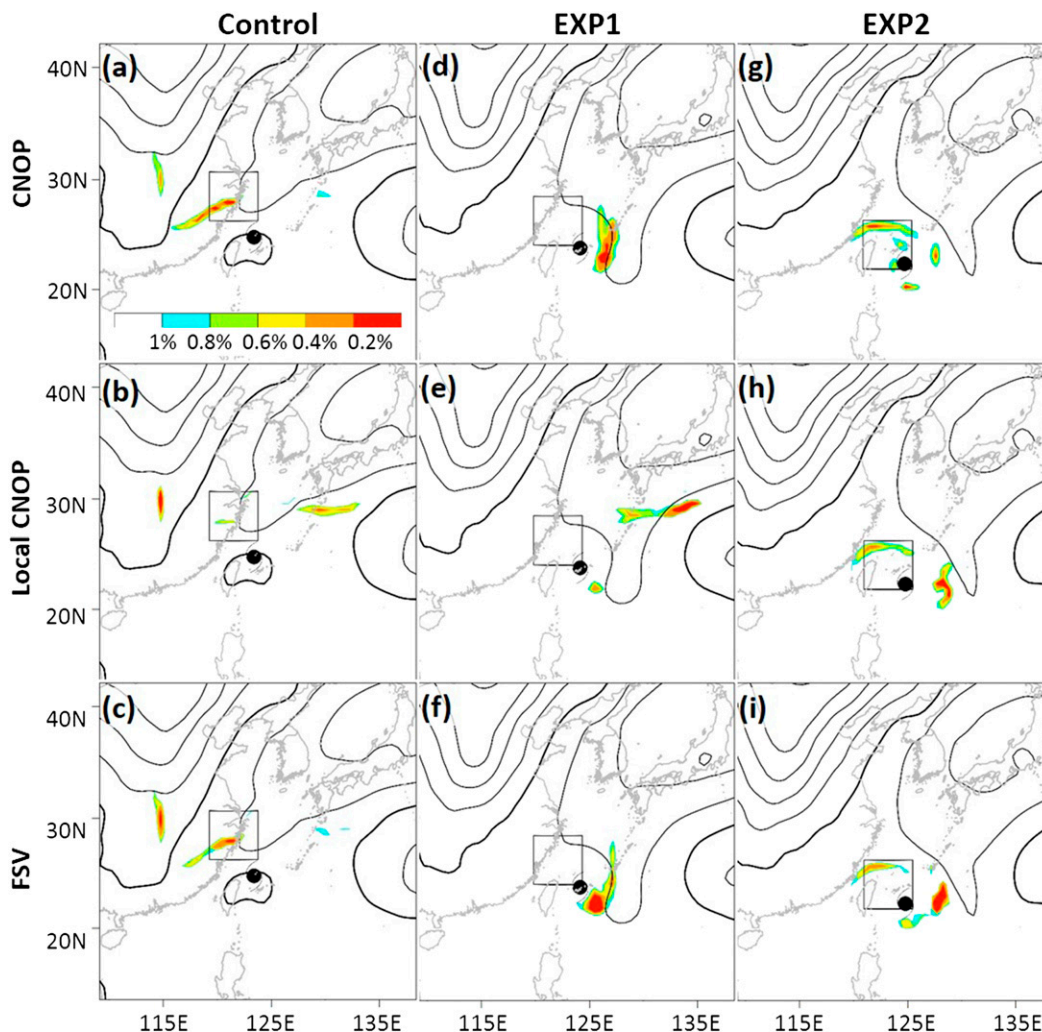


FIG. 14. The geopotential height (contour; m) and the sensitive area (shaded) at the initial time, at 200 hPa of the (a),(d),(g) CNOP, (b),(e),(h) local CNOP, and (c),(f),(i) FSV for the (a)–(c) control experiment, (d)–(f) EXP1, and (g)–(i) EXP2.

the verification area. The results also showed that the three types of perturbations had different capabilities in capturing important influential weather systems for the TDE forecast metric. The local CNOP method captured the signal earlier than the CNOP and FSV methods. All three perturbation methods identified similar sensitive regions when the typhoon was close to or far away from other systems. When the distance was neither too far nor too close, the local CNOP method captured the signal from the subtropical high, while the CNOP and FSV methods did not.

Finally, it is important to note that the case study results in this reported work just demonstrated the likely patterns in the horizontal and vertical distributions of perturbations and the sensitive areas in the two cases. These features may change in different cases.

The limitations of the FSIP system include the limited choices of physical parameterization schemes in the WRFPLUS package and the nonparallel computational algorithm. This system will be updated with the improvement of the WRFPLUS.

Acknowledgments. This work was partially supported by the National Key Basic Research and Development Project of China (HY and ZM; Grant 2013CB430104), the China Special Fund for Meteorological Research in the Public Interest (HY and ZM; Grant GYHY201306004), National Natural Science Foundation of China (HY and ZM; Grants 41375048, 41425018, 41461164006), and the “111-Plan” Project of China (Grant B17049). The authors also thank Yuanfu Xie for the discussion regarding the optimization algorithm, and Ke Zhong and Jianyu Liu for

their help in developing some IO interfaces in the FSIP tool.

APPENDIX

A Brief Introduction to the Configuration of the FSIP System

a. README of the namelist file for the two modules

```
#!/bin/bash
# This Shell was initialized by Huizhen Yu
in 07/2014 to run CNOP and FSV automatically
#
# 1. Definition
#-----
#.. 1.1 define work directory path
declare -r work_dir="/vol6/home/pkuswans/usr/yuhz/WRF_CNOP"
declare -r
wrfplus_dir="/vol6/home/pkuswans/usr/yuhz/WRF/WRF3.6.1/WRFPLUSV3"
#.. 1.2 define the way to run
declare -r run="yhrun -n 12 -p TH_NEW1 ./wrf.exe"
#.. 1.3 define wrf experiment parameters
max_dom=1
start_time=(2000 01 24 00 00) # start time
in year month day hour minute
end_time=(2000 01 24 06 00) # end time
in year month day hour minute
interval_time=6 # wrf run time (hours)
interval_input=21600 # wrf boundary file
interval time (second)
interval_output=360 # wrf output interval
(minute)
wrf_dt=600 # wrf run time step
wrf_dx=180000 # horizontal resolution
wrf_dy=180000 # horizontal resolution
e_we=43 # domain grids in west-east
e_sn = 31 # domain grids in south-north
e_vert=21 # vertical levels
p_top = 5000 # the top pressure in Pa
# define the physical schemes we choose in the
forecast
mp_physics=0
ra_lw_physics=0
ra_sw_physics=0
sf_sfclay_physics=0
sf_surface_physics=1
bl_pbl_physics=98
cu_physics=0
```

```
# define the verification area and beta value
that controls the initial perturbation
nmax=139284 # dimensions calculated by
nLon*nLat*nLev in module_op.f
i_st=29
i_ed=36
j_st=10
j_ed=20
k_st=1
k_ed=20
beta=60
# define the norm we use
t_scale=1
p_scale=1
q_scale=0
#-----
%%%%%%%%%%%%%%%%%%%%%%%%%%%%%%%%%%%%%%%%%%%%%%%%%%%%%%%%%%%%%%%%%%%%%%%%
%%%%%%%%
# All definitions are done
# Please do not modify the following
!!!!!!!!!!!!!!!!!!!!!!!!!!!!!!
%%%%%%%%%%%%%%%%%%%%%%%%%%%%%%%%%%%%%%%%%%%%%%%%%%%%%%%%%%%%%%%%%%%%%%%%
%%%%%%%%
# 2. Prepare to obtain CNOP and FSV
#-----
#.. 2.1 produce the parameters
...
#.. 2.2 produce the csh files to combine WRF
and SPG2
...
#.. 2.3 produce WRF namelist for nonlinear
model and TL and AD models (just the basic
namelist, modify it when jobs needs)
...
#.. 2.4 link to the wrfplus code
...
#.. 2.5 some prepost before calculating
CNOP and FSV
...
#.. 3. Compile and run the module
...
#-----
echo "Successfully preparation"
echo "go to the folder to compile and run the
module to calculate CNOP and FSV"
exit
```

b. The File structure of the two modules

The module includes four folders named initial, cnop, fsv, and readout. The folder named "initial" provides the base-state forecast and the first-guess of the initial perturbations. The folder named "cnop" calculates the CNOP,

and “fsv” calculates the FSV. The folder named “readout” contains a Fortran program that reads the CNOP and FSV output files and generates files that can be read by the GrADS plotting package. The GrADS package can then be used to produce figures to illustrate the results.

One test case (the winter storm case examined in this paper) is included in the modules with a horizontal resolution of 180 km and an optimization time of 6 h initialized on 24 January 2000.

REFERENCES

- Aberson, S. D., 2003: Targeted observations to improve operational tropical cyclone track forecast guidance. *Mon. Wea. Rev.*, **131**, 1613–1628, doi:10.1175//2550.1.
- , 2011: The impact of dropwindsonde data from the THORPEX Pacific Area Regional Campaign and the NOAA Hurricane Field Program on tropical cyclone forecasts in the Global Forecast System. *Mon. Wea. Rev.*, **139**, 2689–2703, doi:10.1175/2011MWR3634.1.
- Bergot, T., 1999: Adaptive observations during FASTEX: A systematic survey of upstream flights. *Quart. J. Roy. Meteor. Soc.*, **125**, 3271–3298, doi:10.1002/qj.49712556108.
- Birgin, E. G., J. E. Martinez, and R. Marcos, 2001: Algorithm 813: SPG—Software for convex-constrained optimization. *ACM Trans. Math. Software*, **27**, 340–349, doi:10.1145/502800.502803.
- Bishop, C. H., B. J. Etherton, and S. J. Majumdar, 2001: Adaptive sampling with the ensemble transform Kalman filter. Part I: Theoretical aspects. *Mon. Wea. Rev.*, **129**, 420–436, doi:10.1175/1520-0493(2001)129<0420:ASWTET>2.0.CO;2.
- Chen, B., 2011: Observation system experiments for Typhoon Nida (2004) using the CNOP method and DOTSTAR data. *Atmos. Ocean. Sci. Lett.*, **4**, 118–123, doi:10.1080/16742834.2011.11446914.
- , M. Mu, and X. Qin, 2013: The impact of assimilating dropwindsonde data deployed at different sites on typhoon track forecasts. *Mon. Wea. Rev.*, **141**, 2669–2682, doi:10.1175/MWR-D-12-00142.1.
- Duan, W., M. Mu, and B. Wang, 2004: Conditional nonlinear optimal perturbations as the optimal precursors for ENSO events. *J. Geophys. Res.*, **109**, D23105, doi:10.1029/2004JD004756.
- Grell, G. A., J. Dudhia, and D. R. Stauffer, 1995: A description of the fifth-generation Penn State/NCAR Mesoscale Model (MM5). NCAR Tech. Note NCAR/TN-398+STR, 121 pp.
- Hamill, T. M., F. Yang, C. Cardinali, and S. J. Majumdar, 2013: Impact of targeted winter storm reconnaissance dropwindsonde data on midlatitude numerical weather predictions. *Mon. Wea. Rev.*, **141**, 2058–2065, doi:10.1175/MWR-D-12-00309.1.
- Jiang, Z., and D. Wang, 2012: Conditional nonlinear optimal perturbations: Behaviour during the evolution of cold vortices over northeast China. *Quart. J. Roy. Meteor. Soc.*, **138**, 198–208, doi:10.1002/qj.913.
- Kerswell, R. R., C. C. T. Pringle, and A. P. Willis, 2014: An optimization approach for analysing nonlinear stability with transition to turbulence in fluids as an exemplar. *Rep. Prog. Phys.*, **77**, 085901, doi:10.1088/0034-4885/77/8/085901.
- Langland, R. H., and Coauthors, 1999: The North Pacific Experiment (NORPEX-98): Targeted observations for improved North American weather forecasts. *Bull. Amer. Meteor. Soc.*, **80**, 1363–1384, doi:10.1175/1520-0477(1999)080<1363:TNPEXT>2.0.CO;2.
- Lorenz, E. N., 1963: Deterministic nonperiodic flow. *J. Atmos. Sci.*, **20**, 130–141, doi:10.1175/1520-0469(1963)020<0130:DNF>2.0.CO;2.
- , 1975: Climate predictability. The physical basis of climate modeling, Global Atmospheric Research Programme Publication Series 16, WMO, 132–136.
- Mu, M., and W. Duan, 2003: A new approach to studying ENSO predictability: Conditional nonlinear optimal perturbation. *Chin. Sci. Bull.*, **48**, 1045–1047, doi:10.1007/BF03184224.
- , and Z. Zhang, 2006: Conditional nonlinear optimal perturbations of a two-dimensional quasigeostrophic model. *J. Atmos. Sci.*, **63**, 1587–1604, doi:10.1175/JAS3703.1.
- , and Z. Jiang, 2008a: A method to find perturbations that trigger blocking onset: Conditional nonlinear optimal perturbations. *J. Atmos. Sci.*, **65**, 3935–3946, doi:10.1175/2008JAS2621.1.
- , and —, 2008b: A new approach to the generation of initial perturbations for ensemble prediction: Conditional nonlinear optimal perturbation. *Chin. Sci. Bull.*, **53**, 2062–2068, doi:10.1007/s11434-008-0272-y.
- , W. Duan, and B. Wang, 2003: Conditional nonlinear optimal perturbation and its applications. *Nonlinear Processes Geophys.*, **10**, 493–501, doi:10.5194/npg-10-493-2003.
- , H. Wang, and F. Zhou, 2007: A preliminary application of conditional nonlinear optimal perturbations to adaptive observation. *Chin. J. Atmos. Sci.*, **31**, 1102–1112.
- , F. Zhou, and H. Wang, 2009: A method for identifying the sensitive areas in targeted observations for tropical cyclone prediction: Conditional nonlinear optimal perturbation. *Mon. Wea. Rev.*, **137**, 1623–1639, doi:10.1175/2008MWR2640.1.
- , W. Duan, D. Chen, and W. Yu, 2015: Target observations for improving initialization of high-impact ocean-atmospheric environmental events forecasting. *Natl. Sci. Rev.*, **2**, 226–236, doi:10.1093/nsr/nwv021.
- Palmer, T. N., R. Gelaro, J. Barkmeijer, and R. Buizza, 1998: Singular vectors, metrics, and adaptive observations. *J. Atmos. Sci.*, **55**, 633–653, doi:10.1175/1520-0469(1998)055<0633:SVMAAO>2.0.CO;2.
- Peng, M. S., and C. A. Reynolds, 2005: Double trouble for typhoon forecasters. *Geophys. Res. Lett.*, **32**, L02810, doi:10.1029/2004GL021680.
- , and —, 2006: Sensitivity of tropical cyclone forecasts as revealed by singular vectors. *J. Atmos. Sci.*, **63**, 2508–2528, doi:10.1175/JAS3777.1.
- Qin, X., and M. Mu, 2012: Influence of conditional nonlinear optimal perturbations sensitivity on typhoon track forecasts. *Quart. J. Roy. Meteor. Soc.*, **138**, 185–197, doi:10.1002/qj.902.
- , W. Duan, and M. Mu, 2013: Conditions under which CNOP sensitivity is valid for tropical cyclone adaptive observations. *Quart. J. Roy. Meteor. Soc.*, **139**, 1544–1554, doi:10.1002/qj.2109.
- Reynolds, C. A., and T. E. Rosmond, 2003: Nonlinear growth of singular-vector-based perturbations. *Quart. J. Roy. Meteor. Soc.*, **129**, 3059–3078, doi:10.1256/qj.02.193.
- Skamarock, W. C., and Coauthors, 2008: A description of the Advanced Research WRF version 3. NCAR Tech. Note NCAR/TN-475+STR, 113 pp., doi:10.5065/D68S4MVH.
- Snyder, C., 1996: Summary of a workshop on adaptive observation and FASTEX. *Bull. Amer. Meteor. Soc.*, **77**, 953–961.
- Wang, H., 2009: Application of conditional nonlinear optimal perturbation to mesoscale predictability and targeted observations.

- Ph.D. thesis, Institute of Atmospheric Physics, Chinese Academy of Sciences, 199 pp.
- , M. Mu, and X.-Y. Huang, 2011: Application of conditional non-linear optimal perturbations to tropical cyclone adaptive observation using the Weather Research Forecasting (WRF) model. *Tellus*, **63A**, 939–957, doi:[10.1111/j.1600-0870.2011.00536.x](https://doi.org/10.1111/j.1600-0870.2011.00536.x).
- Wu, C. C., J. H. Chen, P. H. Lin, and K. H. Chou, 2007: Targeted observations of tropical cyclone movement based on the adjoint-derived sensitivity steering vector. *J. Atmos. Sci.*, **64**, 2611–2626, doi:[10.1175/JAS3974.1](https://doi.org/10.1175/JAS3974.1).
- , S. G. Chen, J. H. Chen, K. H. Chou, and P. H. Lin, 2009a: Interaction of Typhoon Shanshan (2006) with the midlatitude trough from both adjoint-derived sensitivity steering vector and potential vorticity perspectives. *Mon. Wea. Rev.*, **137**, 852–862, doi:[10.1175/2008MWR2585.1](https://doi.org/10.1175/2008MWR2585.1).
- , and Coauthors, 2009b: Intercomparison of targeted observation guidance for tropical cyclones in the northwestern Pacific. *Mon. Wea. Rev.*, **137**, 2471–2492, doi:[10.1175/2009MWR2762.1](https://doi.org/10.1175/2009MWR2762.1).
- Zhang, X., X.-Y. Huang, and N. Pan, 2013: Development of the upgraded tangent linear and adjoint of the Weather Research and Forecasting (WRF) model. *J. Atmos. Oceanic Technol.*, **30**, 1180–1188, doi:[10.1175/JTECH-D-12-00213.1](https://doi.org/10.1175/JTECH-D-12-00213.1).
- , —, J. Liu, J. Poterjoy, Y. Weng, F. Zhang, and H. Wang, 2014: Development of an efficient regional four-dimensional variational data assimilation system for WRF. *J. Atmos. Oceanic Technol.*, **31**, 2777–2794, doi:[10.1175/JTECH-D-13-00076.1](https://doi.org/10.1175/JTECH-D-13-00076.1).
- Zhang, X.-Y., H. Wang, X.-Y. Huang, F. Gao, and N. A. Jacobs, 2015: Using adjoint-based forecast sensitivity method to evaluate TAMDAR data impacts on regional forecasts. *Adv. Meteor.*, **2015**, 427616, doi:[10.1155/2015/427616](https://doi.org/10.1155/2015/427616).
- Zou, X., F. Vandenberghe, M. Pondecà, and Y.-H. Kuo, 1997: Introduction to adjoint techniques and the MM5 adjoint modeling system. NCAR Tech. Note NCAR/TN-435-STR, 107 pp.